

# Microscale Sensing with Strongly Interacting NV Ensembles at High Fields

Ainitze Biteri-Uribarren,<sup>1,2</sup> Ana Martin,<sup>1,2</sup> and Jorge Casanova<sup>1,2</sup>

<sup>1</sup>Department of Physical Chemistry, University of the Basque Country UPV/EHU, Apartado 644, 48080 Bilbao, Spain

<sup>2</sup>EHU Quantum Center, University of the Basque Country UPV/EHU, Bilbao, Spain

Advances in sensing devices that utilize NV center ensembles in diamond are driving progress in microscale nuclear magnetic resonance spectroscopy. Utilizing quantum sensing techniques in the high-field regime significantly boosts sensitivity by increasing thermal polarization, and improve spectral quality via enhanced energy shifts. Compatible with the latter, a straightforward manner to further raise sensor sensitivity is to increase NV concentration; although, this intensifies detrimental dipole-dipole interactions among NVs. In this work, we present a method for detecting NMR signals in high-field scenarios while effectively suppressing dipole-dipole couplings in the NV ensemble. Thus, this approach enhances sensitivity by combining highly doped diamond substrates and elevated magnetic fields.

*Introduction.*— Quantum sensors have emerged as tools for detecting magnetic signals in different regimes, spanning pure and applied science [1]. Notably, in the realm of nuclear magnetic resonance (NMR) spectroscopy [2, 3], conventional inductive detection techniques struggle with inherent low sensitivity, limiting their application to millimetre sized samples [4]. On the contrary, quantum sensor-based NMR shows great potential for applications involving minimal sample sizes [4–8] such as high-throughput chemistry [9, 10], single-cell biology [11], and two-dimensional material science [12]. In this context, nitrogen-vacancy (NV) color defects in diamond [4, 5, 13] have gained popularity owing to their performance at ambient conditions, making microscale ensembles of NVs a viable solution to investigate picoliter samples via NMR techniques.

Recently, efforts have concentrated on synthesizing diamonds with a large NV concentration to further enhance NV-based NMR sensitivity [14–23]. This strategy lowers the system’s noise floor, resulting in a higher signal-to-noise ratio (SNR) [24, 25]. In light of this, researchers are designing various mechanisms based on dynamical decoupling techniques (DD) to mitigate detrimental dipole-dipole interactions in highly NV-doped diamonds [19–22, 26]. However, these techniques are not extrapolable to the high-field regime, which is the optimal for operation, as elevated fields amplify the sample-emitted signal due to increased nuclear thermal polarization [27–31].

In this Letter, we introduce SHIELD (Sensing at High field Improved via ELimination of Dipole-dipole), a microwave DD sequence specifically designed for densely packed NV ensembles, capable of operating at high-field conditions. Our sequence simultaneously suppresses dipolar interactions among NVs while coupling the sensor to the high-field NMR signal. Besides, it is robust against common experimental errors such as strain in the diamond lattice, couplings with other impurities in the host substrate, and errors on the applied control drivings. Additionally, our sequence can be incorporated to quantum heterodyne protocols that enable high-resolution sensing [6, 7].

*Theoretical framework.*— We consider a nuclear spin sample placed on top of a diamond with embedded NV centers, in the presence of a large external magnetic field,  $B_z$ ; see Fig. 1. The

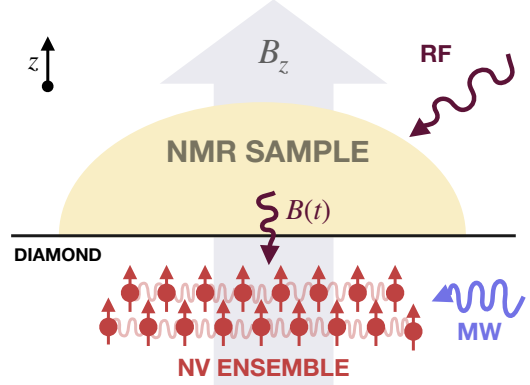


FIG. 1. Illustration of the setup: A [111] cut diamond hosts a dense ensemble of NV centers, exhibiting strong dipole-dipole interactions. A target sample containing nuclear spins is placed on the diamond surface, with a strong magnetic field in the order of Teslas is applied along the  $z$ -axis. Nuclear spins rotate at moderate speed due to an RF field resulting into a slowly oscillating signal,  $B(t)$ , that encodes sample information. Simultaneously, NV centers are controlled using a MW driving.

target NMR signal,  $B(t)$ , is generated by the application of an RF driving on the sample, which bridges the interaction between NVs and nuclear spins. In this manner, even in the high-field regime, the target signal oscillates at a slow rate proportional to the applied RF power [27–30]. Our goal then, is the detection of a slowly oscillating  $B(t)$  with a high density NV ensemble.

The Hamiltonian describing the system reads

$$\frac{H}{\hbar} = \sum_{i=1}^N (\omega + \xi_i) S_i^z + \sum_{i=1}^N \gamma_e B(t) S_i^z + \sum_{i < j}^N H_{dd}^{ij} + \sum_{i=1}^N \Omega \cos(\omega_c t) S_i^\phi, \quad (1)$$

where  $S_i^{z,\phi} = \sigma_i^{z,\phi} / 2$  with  $\sigma_i^\phi = \cos \phi \sigma^x + \sin \phi \sigma^y$ , are the spin operators of the  $i$ -th NV ( $\sigma_i^{x,y,z}$  are Pauli matrices). The first term of the Hamiltonian represents the free energy of  $N$  NV centers, each with a resonance frequency  $\omega = B_z |\gamma_e| + D$ , where  $|\gamma_e| / (2\pi) = 28.024$  GHz/T is the electron gyromagnetic ratio and  $D / (2\pi) = 2.88$  GHz is the NV zero-field splitting. The term  $\xi_i$  accounts for disorder due to lattice strain

or paramagnetic impurities, which introduces variations up to MHz [32] in the NV resonance frequency. The second term describes the interaction between the NV ensemble and the NMR signal  $B(t)$ , and the third term,  $\sum_{i<j}^N H_{dd}^{ij}$ , accounts for dipole-dipole interactions between NVs, see Supplemental Material (SM) [33] for an explicit expression of  $H_{dd}^{ij}$ . The final term corresponds to the microwave (MW) control with amplitude  $\Omega$  and frequency  $\omega_c$ .

In a rotating frame with respect to (w.r.t.)  $H_0 = \sum_{i=1}^N \omega_c S_i^z$ , Eq. (1) reads

$$\frac{H}{\hbar} = \sum_{i=1}^N \xi_i S_i^z + \sum_{i=1}^N [\Delta S_i^z + \Omega S_i^\phi] + \sum_{i=1}^N \gamma_e B(t) S_i^z + \sum_{i<j}^N \bar{H}_{dd}^{ij}, \quad (2)$$

where  $\Delta = \omega - \omega_c$ , and  $\bar{H}_{dd}^{ij} = d_{ij}[S_i^z S_j^z - \frac{1}{2}(S_i^x S_j^x + S_i^y S_j^y)]$ , check SM [33] for further details. Finally, the NMR signal  $B(t) = B_t \cos(\omega t + \phi_t)$  has a frequency  $\omega$ , amplitude  $B_t$ , and initial phase  $\phi_t$ .

We start analyzing the role of dipole-dipole interactions among NV detectors in the widely used Carr-Purcell-Meiboom-Gill (CPMG) protocol [34]. Given that in NV-based NMR experiments, the expectation value  $\sigma^z$  of NV centers is measured, we compute the latter via Eq. (2). In particular, for the CPMG protocol, the system dynamics is described with Eq. (2) by setting  $\Delta = 0$  while  $\Omega$  is deployed stroboscopically. Then, for a cluster of  $q$  interacting NVs we have (see SM [33])

$$\langle \sum_{i=1}^q \sigma_i^z \rangle \approx \frac{2\gamma_e B_t |t_s|}{\pi} \cos(\phi_t) \langle \sum_{i=1}^q \sigma_i^x \rangle_{\rho^*}, \quad (3)$$

where  $\rho^*$  is the NV cluster state evolved only under dipole-dipole interactions and  $|t_s|$  is the CPMG sequence duration. The term  $\langle \sum_{i=1}^q \sigma_i^x \rangle_{\rho^*}$  depends on the dipole-dipole interactions and it can be bounded as  $|\langle \sum_{i=1}^q \sigma_i^x \rangle_{\rho^*}| \leq q$ , achieving its maximum  $q$  in the absence of dipole-dipole couplings. To illustrate this concept, we analytically solved a scenario involving two NV centers (see SM [33]).

In a scenario with an NV ensemble composed of  $Q$  clusters, each containing  $q_k$  NV centers (where  $k = 1, \dots, Q$ ), the total NV signal is the sum from all clusters:  $\sum_{k=1}^Q \langle \sum_{i=1}^{q_k} \sigma_i^z \rangle$ . Then, the contribution of each cluster to the total NV signal has a factor in the range  $[-q_k, q_k]$ , depending on the structure of dipole-dipole terms within the cluster. This means that (i) Each cluster generates a weaker signal compared to that without dipole-dipole interactions, and (ii) In the total NV signal different clusters can interfere destructively, making signal detection challenging. This highlights the importance of developing protocols that suppress dipolar interactions, especially when working with large NV ensembles, to improve NV coherence times and signal sensitivity, ultimately enhancing the effectiveness of NV-based quantum sensing.

*The protocol.*— Our protocol –SHIELD–, incorporates MW driving blocks that continuously mitigate dipole-dipole interactions among NVs, and  $\pi$ -pulses that suppress disorder terms  $\xi_i$  while simultaneously coupling the NV ensemble to  $B(t)$ ; refer to Figure 2 (a) for a scheme of our sequence. The MW

driving blocks generate concatenated  $2\pi$  rotations of the NVs along the axes  $A$ ,  $B$ ,  $\bar{A} = -A$ , and  $\bar{B} = -B$ , which are introduced by setting on the MW control the adequate phase  $\phi$  and a detuning of  $\Delta = \pm \sqrt{\Omega/2}$ ; see Eq. (2). This detuning is the Lee-Goldburg (LG) condition [35] that assures continuous elimination of dipole-dipole interactions, see further details in SM [33].

Rotations along  $A$ ,  $B$ ,  $\bar{A}$ , and  $\bar{B}$  can be combined in different manners. These include the frequency-switched LG sequence [36], which corresponds to the block  $A\bar{A}\bar{A}\bar{A}$ ; and the LG4 sequence  $A\bar{A}\bar{B}\bar{B}$  [37], where the  $B$  axis is rotated an angle  $2\alpha = 110^\circ$  along  $z$  relative to  $A$ . This is, if rotations around  $A$  are exerted with  $\sum_{i=1}^N [\Delta S_i^z + \Omega S_i^\phi]$ ,  $B$  uses  $\sum_{i=1}^N [\Delta S_i^z + \Omega S_i^{\phi+2\alpha}]$ .

Tuning the MW control in Eq. (2) for either the  $A\bar{A}\bar{B}\bar{B}$  or  $A\bar{A}\bar{A}\bar{A}$  block results in the propagator

$$U_c = \exp\left[-i \sum_j^N f_r \sigma_j^C \int_{t_c} \frac{\xi_j + \gamma_e B(t)}{2} dt\right], \quad (4)$$

see SM [33] for the derivation. For simplicity, Eq. (4) assumes complete cancellation of the dipole-dipole term; the validity of this assumption is later verified through numerical analysis. In Eq. (4),  $t_c$  represents the time window during which the MW block is applied, and  $f_r$  and  $\sigma_j^C$  are the reduction factor and an operator of the  $j$ -th NV around axis  $C$ , which bisects  $A$  and  $B$ , see Fig. 2 b). Both quantities  $-f_r$  and  $\sigma_j^C$ , depend on the chosen configuration for the MW control (see SM [33] for analytical expressions). In particular, the reduction factor has a value of  $f_r = 0.4292$  for the MW block  $A\bar{A}\bar{B}\bar{B}$ , and  $f_r = 0.5774$  for the block  $A\bar{A}\bar{A}\bar{A}$ .

The sequence is completed by introducing  $\pi$ -pulses in a direction perpendicular to axis  $C$ . As  $C$  lays in the  $zy$  plane, see Fig. 2 b),  $\pi$  pulses can be delivered along  $x$ , and the corresponding propagator is  $U_\pi^x = \prod_{j=1}^N (-i)\sigma_j^x$ . These pulses imprint a modulation function  $F(t) = +1, -1$  on  $\sigma_j^C$ , alternating their sign with each pulse. This modulation serves the dual purpose of coupling the NV ensemble with  $B(t)$  as well as of removing the disorder  $\xi_j$ . Consequently, the full sequence reads

$$U = [U_\pi^x (U_c)^m U_\pi^x (U_c)^m]^M = \exp\left[-i \sum_j^N f_r \sigma_j^C \int_{t_s} \frac{\gamma_e B(t) F(t) + \xi_j F(t)}{2} dt\right], \quad (5)$$

where  $m$  defines the number of repetitions of the MW blocks between  $\pi$  pulses (i.e. of  $U_c$ ), while  $M$  being the number of sequence repetitions. Besides,  $t_s$  is the time interval for the application of the protocol, with length  $|t_s| = MT$ . Following a procedure similar to that in Eq. (S13-S18) in SM [33], the above propagator simplifies to

$$U = \exp\left\{-i \frac{\gamma_e B_t |t_s| f_r}{\pi} \cos(\phi_t) \sum_j^N \sigma_j^C\right\}. \quad (6)$$

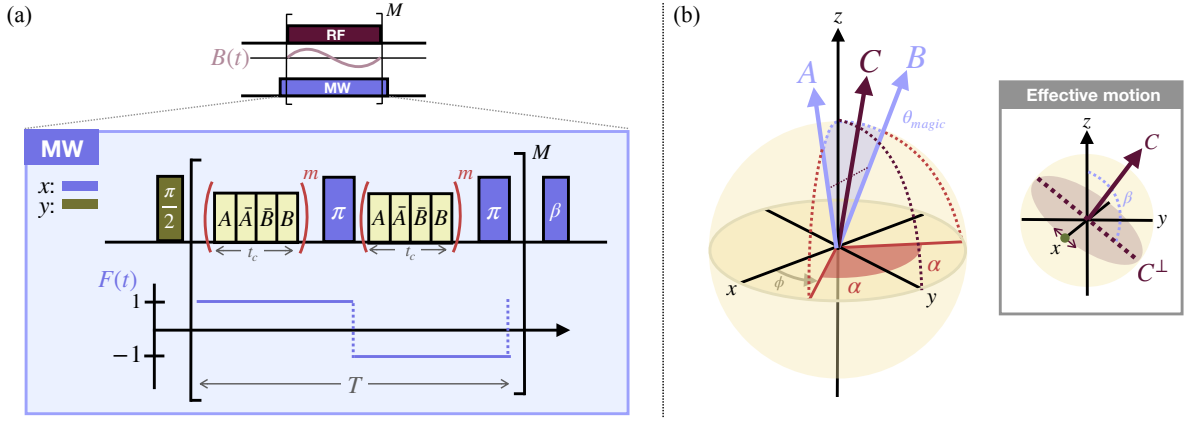


FIG. 2. Scheme of the protocol. (a) At the top, continuous RF driving induces Rabi oscillations of the sample nuclei, which results in the NMR signal  $B(t)$ . At the bottom, the blue square represents the MW pattern of our sequence SHIELD, which simultaneously captures  $B(t)$  while suppressing dipole-dipole interactions. SHIELD includes an initial and final pulse, and in between,  $M$  repetitions of two  $m$  blocks of rotations around the axes  $A, \bar{A}, \bar{B}, B$ , interspersed by  $\pi$ -pulses along the  $x$ -axis. These pulses imprint the function  $F(t)$  with periodicity  $T$  on the effective operators  $\sigma_j^C$ . (b) Relevant direction and angles. In the  $XY$  plane, the axes  $A$  and  $B$  are rotated by angles  $-\alpha$  and  $\alpha$  from the  $y$ -axis about the  $z$ -axis, and both axes  $-A$  and  $B$  form the magic angle with the  $z$ -axis. The effective propagator in Eq. (6) lies along axis  $C$ , which bisects  $A$  and  $B$ . The grey box illustrates the effective dynamics of the NV spins: the initial pulse polarizes the NV centers along the  $x$ -axis (green dot), then the MW scheme slightly rotates the initial state around  $C$ , inducing changes in  $\langle S^{C^\perp} \rangle$ , where  $C^\perp = C \times x$ . For readout, the accumulated spin polarization along  $C^\perp$  is transferred to  $z$ -axis via the final pulse of angle  $\beta$  along the  $x$ -direction.

In addition, note that the initial  $\frac{\pi}{2}$  pulse in Fig. 2 (a) prepares the NV ensemble in the state  $\rho_0 = \bigotimes_j^N (\mathbb{1} + \sigma_j^x)$ , while a final pulse of an angle  $\beta$  along  $x$  transfers the NV population from  $C^\perp$  to the  $z$ -axis for measurement, see Figure 2. b). Then, one can compute the spin population for  $q$  interacting NVs after the application of the protocol as

$$\langle \sum_{i=1}^q \sigma_i^z \rangle = \text{Tr} \left[ U \rho_0 U^\dagger \sum_j^q \sigma_j^C \right] \approx \frac{2\gamma_e B_t |t_s|}{\pi} f_r \cos(\phi_t) q. \quad (7)$$

Comparing the latter to the CPMG signal in Eq. (3), we observe two key differences. First, as a direct consequence of the dipole-dipole canceling mechanism, our protocol introduces the reduction factor  $f_r$  in the signal amplitude; second, the elimination of dipole-dipole interactions allows for all clusters to contribute constructively to the total signal. In other words, the term  $\langle \sum_{i=1}^q \sigma_i^x \rangle_{\rho^*}$  in Eq. (3) converges to the upper bound  $\frac{q}{2}$  for each cluster, resulting in  $\frac{N}{2}$  when accounting for the whole NV ensemble. Therefore, SHIELD enables to leverage highly doped diamonds for increased sensitivity in signal detection, at the cost of introducing the  $f_r$  factor.

Besides, the protocol is versatile: by adjusting the number  $m$  of MW blocks between  $\pi$ -pulses in the sequence of Fig. 2 (a), it enables the detection of target signals across a broad frequency range. From a technical perspective, the delivered  $\pi$  pulses induce a modulation function  $F(t)$  with a period  $T = 4m/\Omega$ , which can be tuned changing  $m$ . Then, via the first harmonic of  $F(t)$ , NVs couple to NMR signals with frequency  $\sim 1/T$ , which can take values from tens of kHz to MHz. In particular, the lower range (kHz) allows for high-resolution NMR signal detection in a high-field scenario, where the sample-NV interaction is mediated by an RF

field [27–30]; while the higher range (MHz) corresponds to medium-field NMR, where SHIELD excels integrated in heterodyne schemes [38]. In contrast, other methods for highly doped diamonds [18–23] are limited to a narrower frequency range in the MHz regime, limiting their application to medium field NMR.

*Numerical results.*— To assess the performance of SHIELD, we conducted numerical simulations for the particularly interesting high-field scenario. Constrained by computational resources, simulations are limited to clusters of up to six dipolar-coupled NVs, over which distinct MW detection schemes are applied. In particular, the clusters couple to a NMR signal via (i) SHIELD with a  $A\bar{A}\bar{B}B$  MW block, (ii) SHIELD with a  $A\bar{A}\bar{A}\bar{A}$  MW block, and (iii) a standard CPMG sequence. To carry out the comparison between these schemes, we evaluate the average NV spin population across hundreds of clusters (i.e.,  $Q \approx 200$ ) as

$$\bar{\sigma}^z = \frac{1}{Q} \sum_{k=1}^Q \frac{1}{q_k} \langle \sum_{i=1}^{q_k} \sigma_i^z \rangle, \quad (8)$$

for systems with different NV densities. Further details are provided in SM [33].

The simulations are performed using Eq. (2) as starting point, dressed with realistic noise effects. Specifically, the MW driving has an amplitude of  $\Omega/(2\pi) = 20$  MHz, with a %1 constant Rabi error applied to both the  $\pi$ -pulses and MW blocks. Detuning errors in the driving are incorporated into the disorder shifts  $\xi_j$ , which also encompass dipolar interactions with misaligned NVs, interactions with other spins in the lattice, and strain in the diamond. These shifts are modeled using a Gaussian distribution centered at 0 with a stan-

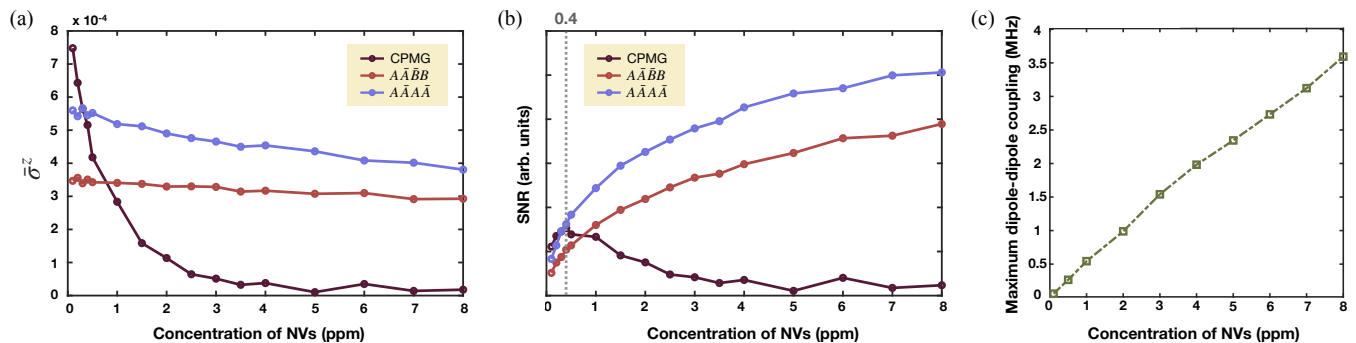


FIG. 3. Numerical results. In every graph, the NV density in the  $x$ -axis corresponds to the concentration of NV centers aligned with the external magnetic field. Note this is the preferential alignment in [111] diamond cuts [39–43]. (a) Oscillation amplitude of  $\bar{\sigma}^z$  for different NV concentrations. Purple curve corresponds to the CPMG protocol, while red and blue curves to SHIELD using the  $A\bar{A}\bar{B}\bar{B}$  and  $A\bar{A}\bar{A}\bar{A}$  MW blocks, respectively. (b) Expected SNR considering projection noise. For CPMG sequence, at 0.4 ppm is reached the best sensitivity, while SHIELD protocols exhibit an increasing tendency of SNR for sensible concentrations. (c) Maximum dipole-dipole coupling, i.e.,  $d_{ij}/(2\pi)$ , at different NV concentrations. This is computed by averaging the maximum dipole-dipole interaction over thousands of distinct configurations, each constituted, on average, by four NVs.

standard deviation of 4 MHz. The NMR signal  $B(t)$  has frequency  $\omega_l/(2\pi) = 95.68$  kHz and an amplitude  $B_l = 1$  nT. The latter corresponds to the thermal polarization of protons in a microscale pure ethanol sample under  $B_z \sim 2$  T [27]. Additionally,  $m = 32$  and  $M = 2$ , as the NV center decoherence time under dynamical decoupling ( $T_2 \sim 20 \mu\text{s}$ ) permits the detection of two oscillations of  $B(t)$ , which last  $t_s = 21 \mu\text{s}$ .

In Fig. 3, we present the numerical outcomes. The first plot (a) shows the amplitude of  $\bar{\sigma}^z$  at various NV concentrations, and the second plot (b) illustrates the corresponding SNR, accounting for projection noise (see SM [33]). The SNR is computed because it reflects the advantages of higher NV concentration; namely, a larger number of NV sensors significantly reduces projection noise.

Analyzing the outcome for the CPMG case, in Fig. 3 (a), we observe a decay in signal amplitude as NV concentration grows, making dipole-dipole interactions stronger, see Fig. 3 (c). Consequently, in Fig. 3 (b), we observe a sensitivity sweet spot for the CPMG. This is, for low NV density, the SNR improves with NV concentration, benefiting from the increasing of NV sensors, until the dipole-dipole interaction among NVs becomes overly strong, causing a rapid decay at 0.4 ppm. Then, according to our simulations, this is the optimal concentration for the CPMG scheme; nevertheless, further numerical analysis suggests that 0.4 ppm would serve as an upper bound (see SM [33]).

Concerning SHIELD protocols, in Fig. 3 (a), they exhibit minimal decay, indicating significant suppression of dipole-dipole interactions. In this regard, note that the SHIELD sequence incorporating the  $A\bar{A}\bar{A}\bar{A}$  block exhibits greater amplitude compared to the  $A\bar{A}\bar{B}\bar{B}$  configuration, although the latter demonstrates superior robustness, characterized by a slower decay. Moving to Fig. 3 (b), this shows that the reduction factor  $f_r$  makes SHIELD protocols unsuitable in scenarios where dipole-dipole interactions among NVs are negligible. However, as the NV concentration increases, the amplitude penalty

from  $f_r$  is compensated by the dipole-dipole cancellation provided by SHIELD. This enables to operate with a large number of NV detectors, resulting in sensitivity levels that exceed those achieved by standard CPMG protocols even at its peak performance.

To further illustrate the comparison, we focus in the case of 5 ppm, where dipole-dipole interactions of 2.5 MHz are observed, see Fig. 3 (c). At this concentration, CPMG suffers a drastic reduction in the signal amplitude, while SHIELD sequences are almost unaffected. This leads to sensitivity rates for SHIELD protocols which are four to five times greater than that of the CPMG sequence. From a general point of view, curves in Fig. 3 (b) indicate a growing SNR for SHIELD at sensible NV concentrations, while standard schemes fail.

**Conclusion.** - We present SHIELD, a MW detection scheme tailored for application in highly concentrated NV-based quantum detectors. Our findings indicate that even at common NV concentrations, just above 0.4 ppm, dipole-dipole interactions detrimentally affect standard AC signal detection schemes. In this scenario, we designed SHIELD, which continuously cancels dipole-dipole interactions, and offers a wide operational range regarding target signal frequencies that spans from tens of kHz to MHz. In this window, the lower frequency range is particularly interesting, as it enables the detection of high-field signals through RF mediation. Thus, SHIELD harnesses the sensitivity gains of dense ensembles and high fields, while further dipole-dipole cancellation resulting in enhanced sensitivities is possible by introducing stronger MW drivings.

**Acknowledgements.** - A. B. U. acknowledges the financial support of the IKUR STRATEGY IKUR-IKA-23/04. J. C. acknowledges the Ramón y Cajal (RYC2018-025197-I) research fellowship. Authors acknowledge the Quench project that has received funding from the European Union’s Horizon Europe – The EU Research and Innovation Programme under grant agreement No 101135742, the Spanish Govern-

ment via the Nanoscale NMR and complex systems project PID2021-126694NB-C21, and the Basque Government grant IT1470-22.

- 
- [1] C. L. Degen, F. Reinhard, and P. Cappellaro, *Quantum sensing*. Review of Modern Physics **89**, 035002 (2017).
- [2] A. Abragam, *The Principles of Nuclear Magnetism*. (Oxford University Press, London, 1961).
- [3] M. H. Levitt, *Spin Dynamics: Basics of Nuclear Magnetic Resonance*, 2nd ed. (Wiley, West Sussex, 2008).
- [4] R. D. Allert, K. D. Briegel, and D. B. Bucher, *Advances in nano- and microscale NMR spectroscopy using diamond quantum sensors*. Chemical Communications **58**, 59 (2022).
- [5] R. Schirhagl, K. Chang, M. Loretz, and C. L. Degen, *Nitrogen-Vacancy Centers in Diamond: Nanoscale Sensors for Physics and Biology*. Annual Review of Physical Chemistry **65**, 83 (2014).
- [6] S. Schmitt, T. Gefen, F. M. Stürmer, T. Uden, G. Wolff, C. Müller, J. Scheuer, B. Naydenov, M. Markham, S. Pezzagna, J. Meijer, I. Schwarz, M. Plenio, A. Retzker, L. P. McGuinness, and F. Jelezko, *Submillihertz magnetic spectroscopy performed with a nanoscale quantum sensor*. Science **356**, 832 (2017).
- [7] D. Glenn, D. B. Bucher, J. Lee, M. Lukin, H. Park and R. L. Walsworth, *High-resolution magnetic resonance spectroscopy using a solid-state spin sensor*. Nature **555**, 7696 (2018).
- [8] K. D. Briegel, N. R. von Grafenstein, J. C. Draeger, P. Bläw, R. D. Allert, and D. B. Bucher, *Optical Widefield Nuclear Magnetic Resonance Microscopy*. arXiv:2402.18239 (2024).
- [9] G. M. Whitesides, *The origins and the future of microfluidics*. Nature volume **442** (2006).
- [10] S. M. Mennen, C. Alhambra, C. L. Allen, M. Barberis, S. Berritt, T. A. Brandt, A. D. Campbell, J. Castañón, A. H. Cherney, M. Christensen, D. B. Damon, J. E. de Diego, S. García-Cerrada, P. García-Losada, R. Haro, J. Janey, D. C. Leitch, L. Li, F. Liu, P. C. Lobben, D. W. C. MacMillan, J. Magano, E. McInturff, S. Monfette, R. J. Post, D. Schultz, B. J. Sitter, J. M. Stevens, I. I. Strambeanu, J. Twilton, K. Wang, and M. A. Zajac, *The Evolution of High-Throughput Experimentation in Pharmaceutical Development and Perspectives on the Future*. Organic Process Research and Development **23**, 6 (2019).
- [11] N. R. Neuling, R. D. Allert, and D. B. Bucher, *Prospects of single-cell nuclear magnetic resonance spectroscopy with quantum sensors*. Current Opinion in Biotechnology **83**, 102975 (2023).
- [12] M. Gibertini, M. Koperski, A. F. Morpurgo, and K. S. Novoselov, *Magnetic 2D materials and heterostructures*. Nature Nanotechnology **14** (2019).
- [13] M. W. Doherty, N. B. Manson, P. Delaney, F. Jelezko, J. Wrachtrup, and L. C. L. Hollenberg, *The nitrogen-vacancy colour centre in diamond*. Physical Reports **528**, 1 (2013).
- [14] T. Chakraborty, F. Lehmann, J. Zhang, S. Borgsdorf, N. Wöhr, R. Remfort, V. Buck, U. Köhler, and D. Suter, *CVD growth of ultrapure diamond, generation of NV centers by ion implantation, and their spectroscopic characterization for quantum technological applications*. Physical Review Materials **3**, 065205 (2019).
- [15] O. Dhungel, T. Lenz, M. Omar, J. S. Rebeirro, M. T. Luu, A. T. Younesi, R. Ulbricht, V. Ivády, A. Gali, A. Wickenbrock, and D. Budker, *Near zero-field microwave-free magnetometry with ensembles of nitrogen-vacancy centers in diamond*. Physical Review B **109**, 224107 (2024).
- [16] L. B. Hughes, S. A. Meynell, W. Wu, S. Parthasarathy, L. Chen, Z. Zhang, Z. Wang, E. J. Davis, K. Mukherjee, N. Y. Yao, and A. C. Bleszynski Jayich, *A strongly interacting, two-dimensional, dipolar spin ensemble in (111)-oriented diamond*. arXiv:2404.10075 (2024).
- [17] A. J. Healey, L. T. Hall, G. A. L. White, T. Teraji, M. A. Sani, F. Separovic, J. P. Tetienne, and L. C. L. Hollenberg, *Polarization transfer to external nuclear spins using ensembles of nitrogen-vacancy centers*. Physical Review Applied **15**, 054052 (2021).
- [18] H. Zhou, J. Choi, S. Choi, R. Landig, A. M. Douglas, J. Isoya, F. Jelezko, S. Onoda, H. Sumiya, P. Cappellaro, H. S. Knowles, H. Park, and M. D. Lukin, *Quantum Metrology with Strongly Interacting Spin Systems*. Physical Review X **10**, 031003 (2020).
- [19] J. Choi, H. Zhou, H. S. Knowles, R. Landig, S. Choi, and M. D. Lukin, *Robust Dynamic Hamiltonian Engineering of Many-Body Spin Systems*. Physical Review X **10**, 031002 (2020).
- [20] H. Zhou, L. S. Martin, M. Tyler, O. Makarova, N. Leitao, H. Park, and M. D. Lukin, *Robust Higher-Order Hamiltonian Engineering for Quantum Sensing with Strongly Interacting Systems*. Physical Review Letters **131**, 220803 (2023).
- [21] M. Tyler, H. Zhou, L. S. Martin, N. Leitao, and M. D. Lukin, *Higher-Order Methods for Hamiltonian Engineering Pulse Sequence Design*. Physical Review A **108**, 062602 (2023).
- [22] N. Arunkumar, K. S. Olsson, J. T. Oon, C. A. Hart, D. B. Bucher, D. R. Glenn, M. D. Lukin, H. Park, D. Ham, and R. L. Walsworth, *Quantum Logic Enhanced Sensing in Solid-State Spin Ensembles*. Physical Review Letters **131**, 100801 (2023).
- [23] H. Zhou, H. Gao, N. T. Leitao, O. Makarova, I. Cong, A. M. Douglas, L. S. Martin, and M. D. Lukin, *Robust Hamiltonian Engineering for Interacting Qudit Systems*. Physical Review X **14**, 031017 (2024).
- [24] J. M. Taylor, P. Cappellaro, L. Childress, L. Jiang, D. Budker, P. R. Hemmer, A. Yacoby, R. Walsworth, and M. D. Lukin, *High-sensitivity diamond magnetometer with nanoscale resolution*. Nature Physics **4**, 810 (2008).
- [25] J. F. Barry, J. M. Schloss, E. Bauch, M. J. Turner, C. A. Hart, L. M. Pham, and R. L. Walsworth, *Sensitivity optimization for NV-diamond magnetometry*. Reviews of Modern Physics **92**, 015004 (2020).
- [26] J. T. Oon, S. C. Carrasco, C. A. Hart, G. Witt, V. S. Malinovsky, and R. Walsworth, *Beyond Average Hamiltonian Theory for Quantum Sensing*. arXiv:2410.04296 (2024).
- [27] C. Munuera-Javaloy, A. Tobalina, J. Casanova, *High-Resolution NMR Spectroscopy at Large Fields with Nitrogen Vacancy Centers*. Physical Review Letters, **130**, 133603 (2023).
- [28] D. Daly, S. J. DeVience, E. Huckestein, J. W. Blanchard, J. Cremer, and R. L. Walsworth, *Nutation-based longitudinal-sensing protocols for high-field NMR with nitrogen-vacancy centers in diamond*. Physical Review Applied, **22**, 024043 (2024).
- [29] P. Alsina-Bolívar, A. Biteri-Uribarren, C. Munuera-Javaloy, J. Casanova, *J-coupling NMR Spectroscopy with Nitrogen Vacancy Centers at High Fields*, Physical Review Research **6**, 043017 (2024).
- [30] C. Munuera-Javaloy, A. Tobalina, J. Casanova, *High-Field Microscale NMR Spectroscopy with NV Centers in Dipolarly-Coupled Samples*. arXiv: 2405.12857 (2024).
- [31] J. Meinel, M. Kwon, R. Maier, D. Dasari, H. Sumiya, S. Onoda, J. Isoya, V. Vorobyov, and J. Wrachtrup, *High-resolution nanoscale NMR for arbitrary magnetic fields*. Communications Physics **6**, 302 (2023).
- [32] G. Kucsko, S. Choi, J. Choi, P.C. Maurer, H. Zhou, R. Landig, H. Sumiya, S. Onoda, J. Isoya, F. Jelezko, E. Demler, N.Y. Yao, and M.D. Lukin, *Critical thermalization of a disor-*

- dered dipolar spin system in diamond*. Physical Review Letters, **121**, 023601 (2018).
- [33] Supplemental Material.
- [34] S. Meiboom and D. Gill, *Modified Spin-Echo Method for Measuring Nuclear Relaxation Times*. The Review of Scientific Instruments, **29**, 8 (1958).
- [35] M. Lee, and W. I. Goldberg, *Nuclear-Magnetic-Resonance Line Narrowing by a Rotating rf Field*. Physical Review **140**, 1261 (1965).
- [36] M. Mehring, and J. S. Waught, *Magic-Angle NMR Experiments in Solids*. Physical Review B **5**, 3459 (1972).
- [37] M. E. Halse, and L. Emsley, *Improved Phase-Modulated Homonuclear Dipolar Decoupling for Solid-State NMR Spectroscopy from Symmetry Considerations*, Journal of Physical Chemistry A **117**, 25 (2013).
- [38] Quantum heterodyne schemes involve multiple magnetometries synchronized with an external clock, enabling frequency resolution beyond the limits set by the quantum sensor's decoherence. These schemes require AC magnetometry measurements that show dependency on the phase of the target signal [6], as it occurs when measuring with the CPMG or the DD protocols we present on this paper. This is evident in Eq. (3) and Eq. (7), where  $\phi_i$ —the phase of the target signal—appears explicitly.
- [39] M. Lesik, J.-P. Tetienne, A. Tallaire, J. Achard, V. Mille, A. Gicquel, J.-F. Roch, and V. Jacques, *Perfect preferential orientation of nitrogen-vacancy defects in a synthetic diamond sample*. Applied Physics Letters **104**, 113107 (2014).
- [40] J. Michl, T. Teraji, S. Zaiser, I. Jakobi, G. Waldherr, F. Dolde, P. Neumann, M. W. Doherty, N. B. Manson, J. Isoya, and J. Wrachtrup, *Perfect alignment and preferential orientation of nitrogen-vacancy centers during chemical vapor deposition diamond growth on (111) surfaces*. Applied Physics Letters **104**, 102407 (2014).
- [41] T. Fukui, Y. Doi, T. Miyazaki, Y. Miyamoto, H. Kato, T. Matsumoto, T. Makino, S. Yamasaki, R. Morimoto, N. Tokuda, M. Hatano, Y. Sakagawa, H. Morishita, T. Tashima, S. Miwa, Y. Suzuki, and N. Mizuochi, *Perfect selective alignment of nitrogen-vacancy centers in diamond*. Applied Physics Letters **7**, 055201 (2014).
- [42] T. Miyazaki, Y. Miyamoto, T. Makino, H. Kato, S. Yamasaki, T. Fukui, Y. Doi, N. Tokuda, M. Hatano, and N. Mizuochi, *Atomistic mechanism of perfect alignment of nitrogen-vacancy centers in diamond*. Applied Physics Letters **105**, 261601 (2014).
- [43] C. Osterkamp, M. Mangold, J. Lang, P. Balasubramanian, T. Teraji, B. Naydenov, and F. Jelezko, *Engineering preferentially-aligned nitrogen-vacancy centre ensembles in cvd grown diamond*. Scientific Reports **9**, 1 (2019).

## Supplemental Material

### I. CANCELLATION OF HOMONUCLEAR DIPOLE-DIPOLE INTERACTIONS

The complete form of the dipole-dipole interaction between spins  $S_i$  and  $S_j$  is represented in the spin Hamiltonian by the following expression [S1]:

$$H_{dd}^{ij} = b_{ij} \left[ \vec{S}_i \cdot \vec{S}_j - 3(\vec{S}_i \cdot \vec{n})(\vec{S}_j \cdot \vec{n}) \right], \quad (\text{S1})$$

where the amplitude is given by the *dipole-dipole coupling constant*

$$b_{ij} = (2\pi) \frac{\hbar \mu_0 \gamma_1 \gamma_2}{2r_{ij}^3}. \quad (\text{S2})$$

For NV-NV interaction  $\gamma_1 = \gamma_2 = -28.02$  GHz/T, besides,  $\hbar = 1.05457182 \times 10^{-34} \frac{\text{m}^2 \text{kg}}{\text{s}}$ ,  $\mu_0 = 12.56637 \times 10^{-7} \frac{\text{kgm}}{\text{s}^2 \text{A}^2}$ , and the relative vector is given by  $r_{12}^{\vec{r}} = r_{12} \vec{n}$ . Moving to the rotating frame with respect to the free energy terms  $H_0 = \omega_c (S_i^z + S_j^z)$  allows to simplify the Hamiltonian via a secular approximation given that  $\omega_c \gg b_{ij}$ :

$$\begin{aligned} \bar{H}_{dd}^{ij} &\approx b_{ij} \left\{ (1 - 3n_z^2) S_i^z S_j^z + e^{i2\omega_c (S_i^z + S_j^z) t} \left[ S_i^x S_j^x + S_i^y S_j^y - 3(S_i^x S_j^x n_x^2 + S_i^x S_j^y n_x n_y + S_i^y S_j^x n_y n_x + S_i^y S_j^y n_y^2) \right] \right\} \\ &\approx b_{ij} \left\{ (1 - 3n_z^2) S_i^z S_j^z + (2 - 3n_x^2 - 3n_y^2) \frac{1}{2} [S_i^x S_j^y + S_i^y S_j^x] \right\} = b_{ij} \left\{ (1 - 3n_z^2) [S_i^z S_i^z - \frac{1}{2} (S_i^x S_i^x + S_i^y S_i^y)] \right\} \\ &= d_{ij} [S_i^z S_i^z - \frac{1}{2} (S_i^x S_i^x + S_i^y S_i^y)]. \end{aligned}$$

This is the secular dipole-dipole interaction corresponding to the homonuclear case, where the *secular dipole-dipole coupling constant* is

$$d_{ij} = b_{ij} (1 - 3 \cos^2 \theta), \quad (\text{S3})$$

being  $\theta$  the angle that  $\vec{r}$  forms with  $\hat{z}$ , i.e with the static external field  $B_0$ . Now, if we consider an NV ensemble subjected to detuned MW radiation, in the rotating frame with respect to  $H_0$ , we have that

$$H_I = \sum_{i=1}^N [\Delta S_i^z + \Omega S_i^\phi] + \sum_{i < j}^N \bar{H}_{dd}^{ij}, \quad (\text{S4})$$

where Eq. (2) has been recycled, disregarding the disorder terms and those related to the target field, which are not relevant in this development. In order to see the dynamics, it is convenient to perform a change of basis to

$$\sigma_i^\mu = \cos(\theta) \sigma_i^z + \sin(\theta) \sigma_i^{\hat{\mu}}, \quad \text{and} \quad \sigma_i^{\mu^\perp} = -\sin(\theta) \sigma_i^z + \cos(\theta) \sigma_i^{\hat{\mu}}, \quad (\text{S5})$$

where  $\hat{\mu}$  is the effective direction of the MW radiation, and  $\phi_\mu$  the angle that  $\hat{\mu}$  forms with direction  $x$ , see Fig. S1. Thus,  $\cos(\theta) = \frac{\Delta}{\sqrt{\Delta^2 + \Omega^2}}$  and  $\sin(\theta) = \frac{\Omega}{\sqrt{\Delta^2 + \Omega^2}}$ . Pauli matrices are related to spin operators in the standard manner, this is:  $S_i^\alpha = \sigma_i^\alpha / 2$ . Then, considering the new basis, Eq. (S4) can be rewritten as

$$H_I = \sum_{i=1}^N \gamma \frac{\sigma_i^\mu}{2} + \sum_{i < j}^N \bar{H}_{dd}^{ij}, \quad (\text{S6})$$

where  $\gamma = \sqrt{\Omega^2 + \Delta^2}$  is the amplitude of the effective MW driving in direction  $\hat{\mu}$ . If one moves to a second interaction picture with respect to the driving term ( $H_0^I = \sum_i \frac{\gamma}{2} \sigma_i^\mu$ ), RWA can be invoked assuming that  $d_{ij} \ll \gamma$ , thereby eliminating the non-secular terms. In that case, the Hamiltonian reads

$$H_I^I = \sum_{i < j}^N \frac{d_{ij}}{4} \left[ (\cos^2 \theta - \frac{1}{2} \sin^2 \theta) \sigma_i^\mu \sigma_j^\mu + (\sin^2 \theta - \frac{1}{2} \cos^2 \theta - \frac{1}{2}) \frac{1}{2} [\sigma_i^{\mu^\perp} \sigma_j^{\mu^\perp} + \sigma_i^x \sigma_j^x] \right]. \quad (\text{S7})$$

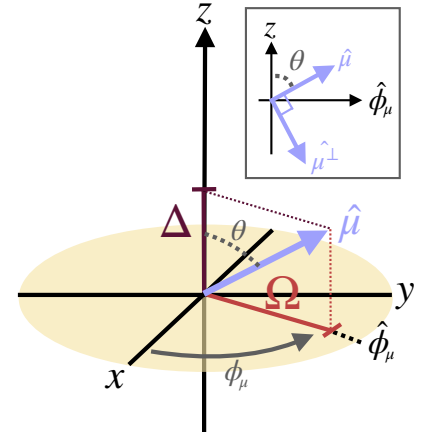


FIG. S1. Illustration of the effective direction of the MW driving  $\hat{\mu}$ , due to the Rabi amplitude in direction  $\hat{\phi}$  and the detuning along  $z$ . The resultant angle that  $\mu$  forms with  $z$  is  $\theta$ . The upper-right inset shows the direction  $\hat{\mu}^\perp$ .

In order to eliminate the dipole-dipole interaction, the trigonometric terms must be set to zero. The angle that nullifies these two expressions at the same time is defined as the *magic angle*

$$\text{if } \theta = \theta_{\text{magic}} = \arccos \frac{1}{\sqrt{3}} \Rightarrow \cos^2 \theta - \frac{1}{2} \sin^2 \theta = \sin^2 \theta - \frac{1}{2} \cos^2 \theta - \frac{1}{2} = 0. \quad (\text{S8})$$

This condition is translated to physical variables as follows: given that  $\cos(\theta) = \frac{\Delta}{\sqrt{\Delta^2 + \Omega^2}}$ , when the deliberate detuning of the MW driving is  $\Delta = \frac{\Omega}{\sqrt{2}}$ , then  $\theta = \theta_{\text{magic}}$ . Hence, to cancel the dipole-dipole interaction, as long as the RWA is satisfied, i.e.,  $d_{ij} \ll \gamma$ , it is sufficient to apply a deliberate detuning that relates to the amplitude of the driving as  $\Delta = \frac{\Omega}{\sqrt{2}}$ , as first documented in [S2].

## II. THE CPMG SEQUENCE IN PRESENCE OF DIPOLE-DIPOLE INTERACTIONS

The CPMG sequence is a widely used pulse sequence for detecting and characterising target AC signals. This protocol consists of a train of  $\pi$  pulses, with a  $\pi/2$  pulse to prepare the initial NV superposition state as well as to finally transfer the achieved phase into populations prior to measurement. To minimize the effect of errors on the drivings, the initial  $\pi/2$  pulse ought to be  $90^\circ$  shifted with respect to the subsequent  $\pi$ -pulses, i.e., for example, the initial  $\pi/2$  pulse around  $-y$ ,  $\pi$  pulses along  $x$  and the last  $\pi/2$  pulse along  $x$ , this is:  $(\pi/2)_{-y} - [(\pi)_x]^n - (\pi/2)_x$ . In such case, to estimate the evolution of the NVs' spin population, one can compute

$$\langle \sum_{i=1}^N S_i^z \rangle = \text{Tr} \left[ U \left[ \bigotimes_j^N (1 + \sigma_j^x) \right] U^\dagger \sum_{i=1}^N S_i^y \right], \quad (\text{S9})$$

where the propagator  $U$  captures the dynamics generated whilst the application of the  $\pi$ -pulses. Note that the initial and final  $\pi/2$  pulses are already implicit in this equation.

The dynamics generated during the  $\pi$ -pulses of the CPMG sequence can be described with Hamiltonian Eq. (2) by setting  $\Delta = 0$  while  $\Omega$  is deployed stroboscopically. This is,

$$H_I/\hbar = \sum_{i=1}^N \Omega(t) S_i^x + \sum_{i=1}^N [\gamma_e B(t) + \xi_i] S_i^z + \sum_{i < j}^N \bar{H}_{dd}^{ij}, \quad (\text{S10})$$

where the driving has been fixed on  $x$ . For the analytical derivation, we assume that the  $\pi$ -pulses of the CPMG protocol are instantaneous and ideal. These pulses leave  $\bar{H}_{dd}^{ij}$  invariant, while imprinting the modulation function  $F(t)$  on the operators  $S_i^z$ . Thus, the Hamiltonian can be rewritten as

$$H_I/\hbar = H_{\text{CPMG}} + \sum_{i < j}^N \bar{H}_{dd}^{ij}, \quad \text{with } H_{\text{CPMG}} = \sum_{i=1}^N \gamma_e B(t) F(t) S_i^z, \quad (\text{S11})$$

where the disorder terms have been neglected: as they are constant in time while the  $\pi$ -pulses alternate the sign of  $S_i^z$ , at the end of the protocol no net effect is accumulated due to them.

Since  $[H_{\text{CPMG}}, \sum_{i < j}^N \bar{H}_{dd}^{ij}] = 0$ , we can treat these terms separately, this is  $U = U_{\text{DD}} U_{\text{CPMG}}$ , where  $U_{\text{DD}}$  and  $U_{\text{CPMG}}$  are the propagators associated to Hamiltonian  $\sum_{i < j}^N \bar{H}_{dd}^{ij}$  and  $H_{\text{CPMG}}$ , respectively. In particular, to compute the expected value for  $\sum_{i=1}^N S_i^z$ , we can separate the dynamics generated by each to ease the computations

$$\langle \sum_{i=1}^N S_i^z \rangle = \text{Tr} \left[ U_{\text{CPMG}} U_{\text{DD}} \rho_0 U_{\text{DD}}^\dagger U_{\text{CPMG}}^\dagger \sum_{i=1}^N S_i^y \right] = \text{Tr} \left[ (U_{\text{DD}} \rho_0 U_{\text{DD}}^\dagger) \left( U_{\text{CPMG}}^\dagger \sum_{i=1}^N S_i^y U_{\text{CPMG}} \right) \right], \quad (\text{S12})$$

where  $\rho_0$  is the state of the NV ensemble prior to the application of the train of  $\pi$ -pulses, i.e.  $\rho_0 = \bigotimes_j^N (1 + \sigma_j^x)$ .

First, we will focus on  $H_{\text{CPMG}}$ . Assume the target field  $B(t)$  is a signal with frequency  $\omega$ , amplitude  $B_t$  and initial phase  $\phi$  at the start of the CPMG protocol, this is  $B(t) = B_t \cos(\omega t + \phi)$ . Additionally, the time separation between the mentioned  $\pi$ -pulses is  $\frac{1}{2\nu}$ , leading to a period  $T = 1/\nu$  on  $F(t)$ . Then,  $F(t)$  can be Fourier expanded as

$$F(t) = \sum_{\kappa \text{ odd}} \frac{4}{\pi \kappa} \cos(\nu \kappa t). \quad (\text{S13})$$

Thus,

$$H_{\text{CPMG}} = \gamma_e B_t \cos(\omega t + \phi) \sum_{\kappa \text{ odd}} \left[ \frac{4}{\pi \kappa} \cos(\nu \kappa t) \right] \sum_{i=1}^N S_i^z. \quad (\text{S14})$$

If the  $\pi$ -pulses are set so  $\nu$  matches the frequency of the target signal, i.e.  $\nu \approx \omega_t$ , only the counter rotating terms of the first harmonic survive. For the rest of the exponents,  $|\omega - \kappa \nu| \gg \gamma_e B_t \frac{4}{\pi \kappa}$ , and of course  $|\omega + \kappa \nu| \gg \gamma_e B_t \frac{4}{\pi \kappa}$ , so they cancel out due to RWA. This is,

$$\begin{aligned} H_{\text{CPMG}} &\approx \frac{\gamma_e B_t}{\pi} \left[ e^{i(\omega-\nu)t} e^{i\phi} + e^{-i(\omega-\nu)t} e^{-i\phi} \right] \sum_{i=1}^N S_i^z \\ &= \frac{2\gamma_e B_t}{\pi} \cos(\delta t + \phi) \sum_{i=1}^N S_i^z \end{aligned} \quad (\text{S15})$$

where  $\delta$  is the difference between the frequency of the target field  $\omega$  and the actual frequency of the modulation function  $\nu$ ,  $\delta = \omega_t - \nu$ , which we assume to be small, of the order of tens of Hertz. Assuming the protocol begins at  $t = 0$  and ends at  $t = t_s$ , its corresponding propagator is

$$U_{\text{CPMG}} = \exp \left\{ -i \int_0^{t_s} H_{\text{CPMG}} dt \right\} \quad (\text{S16})$$

$$= \exp \left\{ -i \frac{2\gamma_e B_t}{\pi \delta} [\sin(\delta t_s + \phi) - \sin(\phi)] \sum_{i=1}^N S_i^z \right\} = \exp \left\{ -i \frac{2\gamma_e B_t}{\pi \delta} [2 \sin(\delta t_s/2) \cos(\delta t_s/2 + \phi)] \sum_{i=1}^N S_i^z \right\}. \quad (\text{S17})$$

Given that  $\delta t_s \ll 1$ , then  $\sin(\delta t_s/2) \sim \delta t_s/2$ ; hence, the propagator can be approximated as

$$U_{\text{CPMG}} = \exp \left\{ -i \frac{2\gamma_e B_t t_s}{\pi} \cos(\delta t_s/2 + \phi) \sum_{i=1}^N S_i^z \right\} \approx \exp \left\{ -i \frac{2\gamma_e B_t t_s}{\pi} [\cos(\phi) + \mathcal{O}(\delta t_s)] \sum_{i=1}^N S_i^z \right\} \quad (\text{S18})$$

$$\approx \exp \left\{ -i \frac{2\gamma_e B_t t_s}{\pi} \cos(\phi) \sum_{i=1}^N S_i^z \right\}. \quad (\text{S19})$$

After obtaining a simplified expression for the propagator, we can compute

$$U_{\text{CPMG}}^\dagger \sum_{i=1}^N S_i^y U_{\text{CPMG}} = \sum_{i=1}^N \exp \left\{ i \frac{4\gamma_e B_t t_s}{\pi} \cos(\phi) S_i^z \right\} S_i^y = \cos \left( \frac{2\gamma_e B_t t_s}{\pi} \cos(\phi) \right) \sum_{i=1}^N S_i^y + \sin \left( \frac{2\gamma_e B_t t_s}{\pi} \cos(\phi) \right) \sum_{i=1}^N S_i^x. \quad (\text{S20})$$

We can now proceed with the target calculation  $\langle \sum_{i=1}^N S_i^y \rangle$ . Given that  $\text{Tr}[(U_{\text{DD}} \rho_0 U_{\text{DD}}^\dagger) \sum_{i=1}^N S_i^y] = 0$ , expression (S12) simplifies to

$$\left\langle \sum_{i=1}^N S_i^z \right\rangle = \sin \left( \frac{2\gamma_e B_t t_s}{\pi} \cos(\phi) \right) \times \sum_{i=1}^N \text{Tr}[(U_{\text{DD}} \rho_0 U_{\text{DD}}^\dagger) S_x^i] \approx \frac{2\gamma_e B_t t_s}{\pi} \cos(\phi) \times \sum_{i=1}^N \text{Tr}[(U_{\text{DD}} \rho_0 U_{\text{DD}}^\dagger) S_x^i], \quad (\text{S21})$$

where, in the second equality, we apply the small angle approximation, given that  $\gamma_e B_t t_s \ll 1$ .

Similarly, in the absence of dipole-dipole interactions among the NV centers, given that  $U_{\text{DD}} = \mathbb{1}$  and  $\text{Tr}[\rho_0 \sum_{i=1}^N S_i^y] = 0$ ,

$$\left\langle \sum_{i=1}^N S_i^z \right\rangle = \text{Tr} \left[ \rho_0 \left( U_{\text{CPMG}}^\dagger \sum_{i=1}^N S_i^y U_{\text{CPMG}} \right) \right] \approx \frac{2\gamma_e B_t t_s}{\pi} \cos(\phi) \times \sum_{i=1}^N \text{Tr}[\rho_0 S_x^i] = \frac{2\gamma_e B_t t_s}{\pi} \cos(\phi) \times N \left( \frac{1}{2} \right). \quad (\text{S22})$$

This is, the dipole-dipole interactions modulate the oscillation amplitude of the NV centers' population with the factor  $|\sum_{i=1}^N \text{Tr}[(U_{\text{DD}} \rho_0 U_{\text{DD}}^\dagger) S_x^i]| \leq N/2$ . Then, in the best-case scenario, with the maximum factor  $N/2$ , dipole-dipole interactions leave the amplitude of the signal unaltered; in all other cases, these interactions lead to detrimental signal attenuation.

For example, considering two NV interaction, i.e.  $N = 2$ , the factor introduced by the dipole-dipole interaction is

$$\sum_{i=1}^{N=2} \text{Tr}[(U_{\text{DD}} \rho_0 U_{\text{DD}}^\dagger) S_x^i] = \cos \left( \frac{3d_{12}}{4} t_s \right). \quad (\text{S23})$$

Hence, this factor achieves a value within the range  $[-1, 1]$ , depending on the strength of the dipolar interaction. Note that this expression is consistent with previous results, as when  $d_{ij} \rightarrow 0$  (there is no dipole-dipole interaction), (S23) achieves its maximum value.

### III. PROPAGATOR OF THE MW BLOCKS

The AC detection protocol we present, interspersed with  $\pi$ -pulses, incorporates MW driving blocks that continuously eliminate dipole-dipole interactions among NVs. In this section, we provide the analytical calculations associated to the MW block to support the formulas in the main text.

The dipole-dipole suppressing MW block consists on four rotations: one around  $A$ , one around its opposite vector  $\bar{A} = -A$ , another around the opposite of  $B$  (this is  $\bar{B} = -B$ ) and a last one around  $B$  (see Fig. 2). In order to see the dynamics, we should define the Hamiltonian governing during each rotation. For that, it is convenient to recycle the basis (S5), where  $\mu$  can be  $A$  or  $B$ , with the corresponding  $\phi_A = 35^\circ$  or  $\phi_B = \phi_A + 2\alpha = 125^\circ$  ( $\alpha = 55^\circ$  is empirically proven to minimize noise), and  $\theta = \theta_{magic}$  (see Fig. S2). Rewriting Eq. (2) in terms of the operators on Eq. (S5):

$$H_I^\mu = \sum_{j=1}^N \frac{\xi_j + \gamma_e B(t)}{2} \cos(\theta_{magic}) \sigma_j^\mu + \sum_{j=1}^N \frac{\gamma}{2} \sigma_j^\mu, \quad (S24)$$

where  $\gamma = \sqrt{\Omega^2 + \Delta^2} = \sqrt{\frac{3}{2}}\Omega$  is the amplitude of the effective MW driving along direction  $\mu$ . For simplicity, the previous equation assumes complete cancellation of the  $\sum_{i < j}^N \bar{H}_{dd}^{ij}$  term. Besides, the terms that go with  $\sigma_i^{\mu\perp}$  have been neglected due to RWA (since  $\frac{\xi_i + \gamma_e B(t)}{2} \ll \gamma$ ). On the other hand, since  $\sigma_j^{\bar{A}} = -\sigma_j^A$  and  $\sigma_j^{\bar{B}} = -\sigma_j^B$ , the Hamiltonian governing during rotations around the opposite axes is

$$H_I^{\bar{\mu}} = \sum_{j=1}^N \frac{\xi_j + \gamma_e B(t)}{2} \cos(\theta_{magic}) \sigma_j^\mu + \sum_{j=1}^N \frac{\gamma}{2} (-\sigma_j^\mu). \quad (S25)$$

Then, the propagator for the MW block is

$$U_{A\bar{A}\bar{B}B} = e^{-i \int_{t_B} H_B dt} e^{-i \int_{t_B} H_B dt} e^{-i \int_{t_A} H_{\bar{A}} dt} e^{-i \int_{t_A} H_A dt} \\ = \exp \left\{ -i \int_{t_B+t_{\bar{B}}}^{t_B} \sum_{j=1}^N \frac{\xi_j + \gamma_e B(t)}{2} \cos(\theta_{magic}) \sigma_j^B dt \right\} \exp \left\{ -i \int_{t_A+t_{\bar{A}}}^{t_A} \sum_{j=1}^N \frac{\xi_j + \gamma_e B(t)}{2} \cos(\theta_{magic}) \sigma_j^A dt \right\}, \quad (S26)$$

where  $t_\mu$  is the time window for which the MW rotation around  $\mu$  occurs. These intervals have a duration  $1/\gamma$  (the required length for a  $2\pi$  rotation). If we assume that  $\gamma \gg |\frac{dB(t)}{dt}|$ , then during subsequent MW rotations the target field  $B(t)$  does not change much, meaning that  $\int_{t_A+t_{\bar{A}}} \delta(t) dt \sim \int_{t_B+t_{\bar{B}}} \delta(t) dt$ , thereby we can approximate with  $\frac{1}{2} \int_{t_A+t_{\bar{A}}+t_B+t_{\bar{B}}} \delta(t) dt$ . Besides, given  $|\delta(t)| \frac{1}{\gamma} \ll 1$ ,

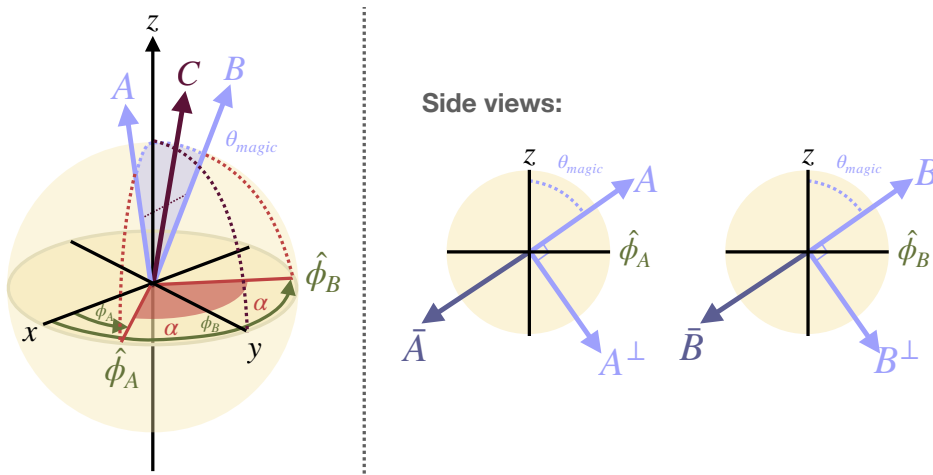


FIG. S2. Illustration showing the pertinent directions and angles to follow the analytical computations. On the left, the 3D scheme, where  $A$  ( $B$ ) forms with  $x$  in the  $XY$  plane an angle  $\phi_A$  ( $\phi_B$ ), defining the directions  $\hat{\phi}_A$  and  $\hat{\phi}_B$ . On the right, side cuts of the sphere showing the planes containing  $z$  and the directions  $\hat{\phi}_\mu$ .

the Baker-Campbell-Hausdorff formula can be truncated to first order, this allows for the approximation of Eq. (S26) as follows

$$U_{A\bar{A}B\bar{B}} \sim \exp \left\{ -i \sum_j^N \left( \int_{t_A+t_{\bar{A}}+t_B+t_{\bar{B}}} \frac{\xi_i + \gamma_e B(t)}{2} dt \right) \cos(\theta_{\text{magic}}) \frac{(\sigma_j^A + \sigma_j^B)}{2} \right\}. \quad (\text{S27})$$

The latter can be rewritten given that  $(\sigma_j^A + \sigma_j^B)/2 = \cos(\theta_{\text{magic}})\sigma_j^z + \sin(\theta_{\text{magic}})\sin\phi_A\sigma_j^y \equiv \sigma_j^C \sqrt{\cos^2(\theta_{\text{magic}}) + \sin^2(\theta_{\text{magic}})\sin^2\phi_A}$ . Thus,  $C$  is the direction of the axis along which the effective MW rotation occurs when radiating the MW block fast enough (i.e. when the aforementioned conditions are met). This is

$$U_{A\bar{A}B\bar{B}} \sim \exp \left\{ -i \sum_j^N f_r \sigma_j^C \int_{t_A+t_{\bar{A}}+t_B+t_{\bar{B}}} \frac{\xi_i + \gamma_e B(t)}{2} dt \right\} \quad (\text{S28})$$

where  $t_A + t_{\bar{A}} + t_B + t_{\bar{B}}$  is the time window for the application of the MW block and  $f_r = \sqrt{\cos^2(\theta_{\text{magic}}) + \sin^2(\theta_{\text{magic}})\sin^2\phi_A} \cos(\theta_{\text{magic}})$  is a reduction factor. This reduction factor is a consequence of the applied continuous driving, which limits the NV centers from fully detecting the target signal, thereby introducing an amplitude penalty. In other words, it is the price to pay in exchange of protection against dipole-dipole interactions, and it depends on the specific sequence. In particular, for the MW block  $A\bar{A}B\bar{B}$ ,  $f_r = 0.4292$ ; while for the frequency switched protocol, with  $\phi_A = 90^\circ$  and  $\alpha = 0$  (hence,  $A = B$  and the applied MW block is  $A\bar{A}A\bar{A}$ ), the reduction factor is  $f_r = \cos\theta_{\text{magic}} = 1/\sqrt{3}$ .

#### IV. NUMERICAL SIMULATIONS

In this work, via numerical simulations, we compare the performance of three AC detection protocols, these are: CPMG, SHIELD utilizing MW block  $A\bar{A}A\bar{A}$  and SHIELD with  $A\bar{A}B\bar{B}$ . Fig. 3 in the main text, presents the final numerical outcomes; and in this section we show the methodology employed to extract the data depicted in that figure.

##### A. High-field detection sequence

To compare the performance of these measurement protocols, we integrate them within the detection scheme AERIS [S27], as they would be employed in high field experimental setups. AERIS is a scheme tailored for high field signals that consists on multiple short-duration NV measurements. In this manner, the NV decoherence does not limit the spectral resolution; instead, the

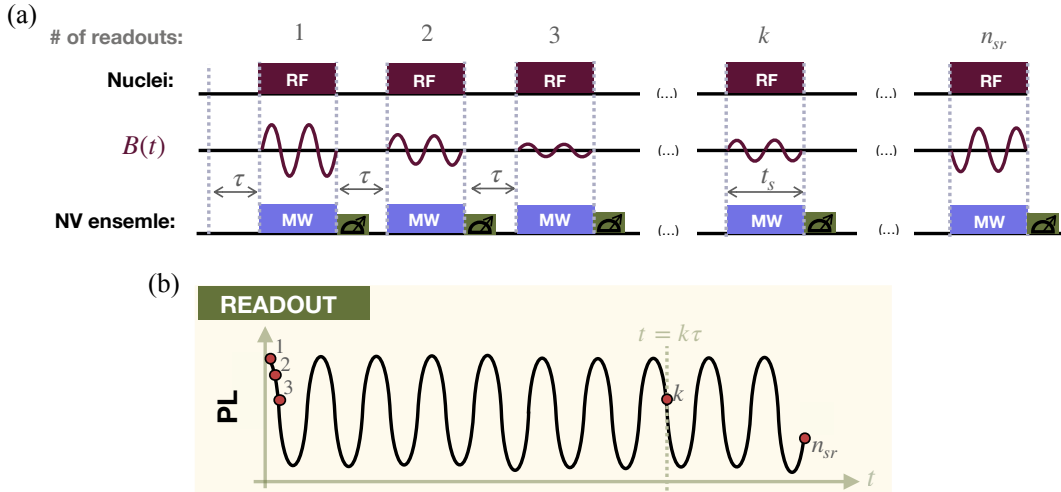


FIG. S3. (a) Illustration of the AERIS detection scheme, which consists of  $n_{sr}$  measurements. In each measurement, a  $2\pi$  rotation is applied to nuclei in the NMR sample via RF, inducing the field  $B(t)$  on the NV ensemble. This field then is simultaneously detected by the NV ensemble using a MW measuring protocol that can be any of the three mentioned in the text. (b) Schematic of the recorded PL signal with the detection scheme. Each red point corresponds to an NV ensemble readout, resulting in oscillations with frequency  $\delta$ .

frequency resolution is dictated by the decoherence of the target signal, just as in heterodyne schemes. During the measurements within AERIS, the NV ensemble captures the RF-induced Rabi oscillations of nuclear spins, which encode chemical information of the NMR sample in the amplitude. These measurements can be carried out through the application of any of the three mentioned measurement protocols. Refer to Fig. S3 for the detection scheme.

For the sake of simplicity, we consider a single chemical shift  $\delta = 200$  Hz as the target parameter. Then, one can show that the magnetic field on the NV ensemble during the  $k$ -th magnetometry measurement reads as

$$B^k(t) = B_t^k \sin(\omega_t t) \quad \text{where} \quad B_t^k = B_t \cos(\delta \tau k), \quad (\text{S29})$$

where  $\tau$  represents the time interval between successive measurements. This is, the amplitude of the magnetic field sensed by the NV ensemble changes from one measurement to the next one; in particular, it varies sinusoidally according to the chemical shift  $\delta$ . Following Eq. (3) and (7), the application of the measurement protocols results in a photoluminescence (PL) signal that is proportional to

$$\left\langle \sum_{j=1}^q \sigma_z^j \right\rangle^k = \frac{2\gamma_e B_t \cos(\delta \tau (k-1)) t_s f_r}{\pi} \times \left\langle \sum_{j=1}^q \sigma_j^x \right\rangle_{\rho^s}, \quad (\text{S30})$$

where  $q$  is the number of NV centers in the cluster. When the selected measuring protocol is the CPMG, the term  $\langle \sum_{j=1}^q \sigma_j^x \rangle_{\rho^s}$  has a varying value in between  $-q$  and  $q$  depending on the dipole-dipole interactions within the cluster and  $f_r = 1$ . For the SHIELD protocol,  $\langle \sum_{j=1}^q \sigma_j^x \rangle_{\rho^s} = q$ , and  $f_r = 0.4292$  for the  $A\bar{A}\bar{B}B$  block and  $f_r = 0.5774$  for the  $A\bar{A}A\bar{B}$ .

Then, performing multiple measurements that take place at different time instants  $\tau k$ , leads to the reconstruction of the sinusoidal behaviour  $\cos(\delta \tau k)$  in the PL signal, see Fig. S3 (b), from where the parameter  $\delta$  can be estimated. The amplitude of the PL signal, and thereby the sensitivity, varies depending on the particular protocol employed for the NV measurement combined with environmental conditions, such as the NV concentration and the strength of the decoupling drivings.

## B. Methodology

In order to compare the performance of the detection protocols, we require a representative signal for each. This is challenging given the computational constraints, as the simulations are restricted to clusters at most six (or eight) interconnected NV centers. Then, to generate reliable representative signals, we average the results across hundreds of random clusters, continuing until the average signal remains stable, indicating that convergence is reached. This approach, within our computational limitations, captures the randomness of NV center positioning and consequent diversity of dipole-dipole coupling structures that give rise to heterogeneous signals.

To create each random cluster, we place 30 NV centers following uniform probability distribution within a volume that would correspond to 30 NV centers if these were periodically arranged. This volume is

$$V(\text{ppm}) = \left( \frac{30 \times 10^6}{8 \times \text{ppm}} \right)^{1/3} \times a^3, \quad (\text{S31})$$

where  $a = 3.57 \times 10^{-10}$  m is the lattice constant of diamond. Besides we impose the restriction that two NV centers cannot occupy the same lattice cell. We then select those NV centers that have fallen within a spherical volume, corresponding on average to 4 NVs. The radius of this sphere is given by

$$r(\text{ppm}) = \left( \frac{4 \times 10^6}{8 \times \text{ppm}} \times \frac{3}{4\pi} \right)^{1/3}, \quad (\text{S32})$$

Only the configurations containing 2 to 6 NV centers are taken as valid; with these, simulations are conducted with the parameters specified in *Numerical results*. Besides  $\delta = 200$  Hz,  $\tau = 10^{-4}$  s and  $n_{sr} = 100$ .

The output corresponding to each cluster is  $\sum_{j=1}^q \langle \sigma_j^z \rangle / q$ , where  $q$  is the number of NVs participating in the respective configuration. This output is then averaged across hundreds of configurations, resulting in  $\bar{\sigma}^z = \frac{1}{Q} \sum_{k=1}^Q \frac{1}{q_k} \langle \sum_{i=1}^{q_k} \sigma_i^z \rangle$ . In particular, the CPMG-integrated protocol is run over  $Q = 400$  clusters, while the SHIELD protocols are run over  $Q = 200$ , as the latter converge faster because the dipole-dipole suppression eliminates the heterogeneity among the configurations. This phenomenon is captured in Fig. S4, where the output signals for 1 ppm are depicted along with a convergence graph (Fig. S4d).

As reported in Fig. S4, every detection scheme yields the expected oscillatory behaviour, with their frequencies directly encoding the target parameter  $\delta$ . The difference in output signals between protocols resides in the amplitude, which is mainly influenced by the reduction factor intrinsic to each scheme and their capability to suppress dipole-dipole interactions. Indeed,

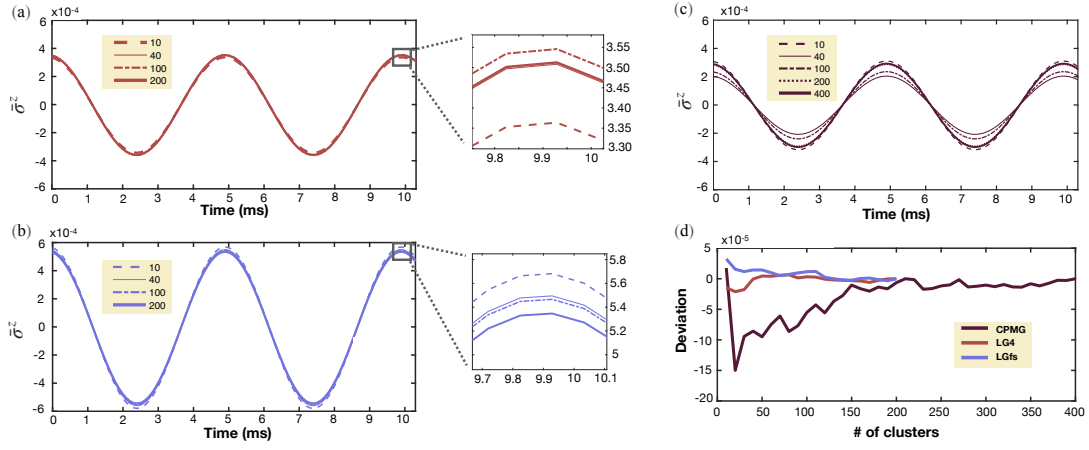


FIG. S4. Simulations of the model at 1 ppm NV concentration. (a)  $\bar{\sigma}^z$  signal captured via AERIS using SHIELD with MW block  $A\bar{A}\bar{I}\bar{I}B\bar{B}$  for detection, after averaging over 10, 40, 100 and 200 clusters. On the right side, there is a zoomed-in view of the signals. The lines corresponding to 40 and 200 clusters fall on top of each other. The converged signal, that corresponding to 200 clusters, is depicted with a continuous thick line. (b) and (c) Equivalent figure showing the results using SHIELD with MW block  $A\bar{A}\bar{A}\bar{A}$  and CPMG, respectively. (d) Convergence graph: the y-axis shows the difference between the oscillation amplitude averaged over a given number of clusters and the oscillation amplitude of the converged signal, while the x-axis represents the number of clusters used for averaging.

the diverse structures of dipole-dipole interactions across different clusters result in different signal amplitudes, even inverting the signal in certain cases. Consequently, when the signals are averaged, they interfere destructively, leading to an effective reduction in the overall signal amplitude. This phenomenon is also expected in experimental settings. When each NV center in the ensemble experiences a different configuration around it and exhibits different spin projection, the net signal is adversely affected, diminishing its amplitude. However, when dipole-dipole interactions are suppressed, which is the case for SHIELD protocols, the variation in the signal across different configurations is much smaller, resulting in almost no reduction in the signal amplitude.

In order to construct Fig. 3 (a), signal convergence was achieved with the three protocols in ensembles containing two to six NV centers, for NV densities with ppm = 0.1, 0.2, 0.3, 0.4, 0.5, 1, 1.5, 2, 2.5, 3, 3.5, 4, 5, 6, 7, and 8. These concentrations correspond to the NV centers aligned with  $B_z$ . Then, Fig. 3 (a) portrays the amplitudes of the converged signals. In other words, these signals correspond to the spin projection of a single referential NV. Taking the latter into account, the SNR is estimated by multiplying  $\sqrt{N}$  by the values on Fig. 3 (a), where  $N$  represents the number of NV centers in the active volume of the diamond  $V_{\text{act}} = 3.14 \times 10^{-15} m^3$  [S7], thus  $N(\text{ppm}) = \text{ppm} \frac{8 \times 10^{-6}}{a^3} V_{\text{act}}$ .

### C. Simulations with larger clusters

The reduced number of constituents we can integrate into the numerical simulations alters the results. For example, the oscillatory behaviour exhibited in Fig. 3 (a) for the sequence with the CPMG protocol, we argue it is a consequence of the restricted amount of interacting NV centers in the simulations; for an infinite amount of interacting NVs we expect a smooth decay. Additionally, we suspect that this numerical condition results non-favorable to our protocol when performing the comparison. This is: the observed advantage of the dipole-dipole protected protocols over the CPMG-integrated version is likely a lower bound. When a bigger volume is considered and more elements are included in the clusters, the potential variations in the arrangement of NVs increase. This leads to a greater diversity of signals across different clusters, resulting in a more pronounced destructive interference in the overall signal. From a more physical point of view, one can think that more interaction channels lead to a faster decay. This phenomena affects much less in the schemes dressed with dipole-dipole suppression, indicating that the comparison carried out is indeed a lower bound of the improvement in sensitivity of the LG-integrated schemes.

In order to gain insight regarding the latter assumption, we run for 1 ppm of NV concentration some simulations with the exact same conditions as before, but with slightly greater clusters. In particular, we select the NV centers that fall in a spherical volume that in average captures six NV centers instead of four, this is

$$r' (\text{ppm}) = \left( \frac{6 \times 10^6}{8 \times \text{ppm}} \times \frac{3}{4\pi} \right)^{1/3}, \quad (\text{S33})$$

and we take as valid those configurations containing two to eight NV centers. The converged signals are shown in Fig. S5, where, for comparison, are also included those corresponding to the smaller cluster. This figure reports the expected behaviour: the outcome for the SHIELD protocol remains relatively stable as the system is expanded. In contrast, for the protocol using CPMG, increasing the number of NV centers has a detrimental effect, even when the concentration remains unchanged.

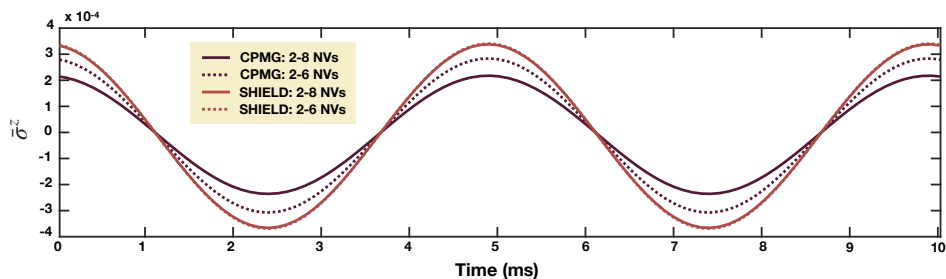


FIG. S5. Converged signals at 1 ppm NV concentration: the continuous lines represent the results from clusters including two to eight NV centers; while the dashed lines show the outcome from the more restricted clusters with two to six NV centers. The same color code as before is used to differentiate the results obtained with the distinct protocols: the purple lines indicate the outcomes using the CPMG detection scheme, whereas the red lines correspond to SHIELD with MW block  $A\bar{A}\bar{B}B$ .

[S1] M. H. Levitt, *Spin Dynamics: Basics of Nuclear Magnetic Resonance*, 2nd ed. (Wiley, West Sussex, 2008).

[S2] Moses Lee, Walter I. Goldberg, *Nuclear-Magnetic-Resonance Line Narrowing by a Rotating rf Field*. Phys. Rev., **140**, 1261 (1965).